Journal of Power Sources 518 (2022) 230714

Contents lists available at ScienceDirect

Journal of Power Sources

journal homepage: www.elsevier.com/locate/jpowsour

Comparison of expansion and voltage differential indicators for battery capacity fade☆

Peyman Mohtat *, Suhak Lee, Jason B. Siegel, Anna G. Stefanopoulou

Mechanical Engineering Department, The University of Michigan, Ann Arbor, Michigan 48109-2125, USA

HIGHLIGHTS

- Expansion of lithium-ion batteries is measured during aging.
- Features in differential expansion are strongly correlated with capacity fade.
- The correlation is nearly linear under a wide range of conditions.
- The feature stays observable up to 1C and is robust to the starting SOC of charge.

GRAPHICAL ABSTRACT

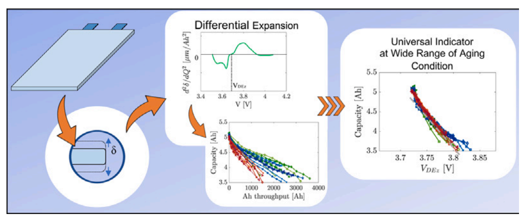

ARTICLE INFO

Keywords:
Lithium-ion
Battery
Expansion
Health estimation

ABSTRACT

The expansion of lithium-ion batteries exhibits characteristic inflection points during cycling that are distinctly identifiable using differential analysis. In this paper, we show that the evolution of several features in the second-differential of expansion correlates to capacity loss under a wide range of stress factors such as temperature, charging rate, and depth-of-discharge. Specifically, the evolution of the zero-crossing point of the second differential of the expansion has a strong correlation with capacity fade. The correlation is nearly linear and universal as the same correlation describes capacity fade for various conditions tested on NMC/Graphite cells. The zero-crossing expansion feature remains observable at higher C-rates up to 1C and is robust when the charging commences from different states of charge. The expansion feature also occurs near the half-charged point. Thus, the expansion measurement can enable fast and more robust capacity estimation at the end of a manufacturing process for quality control, during cycling testing in the lab, or even in the field.

1. Introduction

A consensus has finally taken shape by science, policy, and industry that electric vehicles (EV) should constitute 1/5 of the global vehicle fleet to meet the carbon emission goals of 2030. Consequently, light-duty vehicle manufacturers are preparing for a transition that could bring tens of millions of EVs to the road. With the production of lithium-ion batteries projected to ramp up to billions of cells by the end of the decade, it is necessary to develop diagnostics that estimate the state of health of batteries, assess their condition and residual value to ultimately stretch their lifetime [1]. Accurate knowledge of lithium-ion batteries' health is essential for optimal battery operation with regards to power limits, cycle-life, and safety. The most important aspect of a battery's health is the amount of charge it can store, i.e., the capacity, however, capacity measurement is often challenging in real-world operation since most EVs are rarely deeply discharged due to range anxiety. Moreover, reducing the testing time in the laboratory settings for capacity checks during aging tests is often greatly advantageous in terms of cost reduction (labor, data, equipment, test time).

The state of health (SOH), defined here as capacity retention, can be quantified by full charge–discharge that takes time, which is rarely possible since convenient home and workplace charging will be used to maintain the battery near full levels. Several techniques to estimate

☆ Distribution A. Approved for public release; distribution unlimited. (OPSEC 5301)

* Corresponding author.
E-mail address: pmohtat@umich.edu (P. Mohtat).

https://doi.org/10.1016/j.jpowsour.2021.230714
Received 3 August 2021; Received in revised form 23 October 2021; Accepted 30 October 2021
Available online 18 November 2021

capacity involve parametric estimation simultaneously with state of charge (SOC) estimation using terminal voltage measurements, and Coulomb counting [2–4]. These algorithms converge to the true capacity value when the operation straddles the graphite phase transitions [5]. These are the same phase transitions observed in the differential voltage (DV) analysis [6–8] and incremental capacity (IC) analysis [9] that are used mostly in the laboratory for estimating SOH. These methods track the voltage level where DV peaks are observed and correlate to the capacity as cells degrade. These correlations can be used when the battery is charging under a constant low current, which avoids the confounding influence of impedance. The DV peaks can also provide additional information about the anode capacity and stoichiometric utilization window [10].

An insightful indicator of lithium-ion battery aging is the mechanical expansion during cycling. Lithium-ion batteries are made of electrodes that expand during charging and contract during discharging. The combined cell-level expansion can be characterized either using a strain sensor or a force sensor. For example, when the battery is compressed in a fixture, the intrinsic material swelling is constrained and causes stresses that can be measured as an increase in pressure. Recently, the influence of aging on the swelling has shown promising results for predicting SOH as a function of the cell deformation [11]. It has been also shown that the measurement of the mechanical response can improve the accuracy of SOC estimation [12,13]. The graphite phase transitions are also observable as peaks in the second differential of the expansion. This connection was first reported and explained in [14]. As the cell ages due to the loss of active material (LAM) and loss of lithium inventory (LLI) [15] aging modes, the peaks, and features in the expansion shift. The differential expansion (DE) signal has the advantage of better peak observability at higher C-rates [16] compared to the DV signal. Therefore, the DE can be used to develop SOH estimation methods, either by itself or in conjunction with voltage, to increase the accuracy and robustness [17].

In this work, first, we demonstrate that the features extracted from the expansion during charging at practical rates have a strong correlation with the capacity fade. Furthermore, we directly compare the DV, IC, and various DE features and develop capacity estimation methods based on voltage and expansion that are accurate and robust with respect to the aging conditions. Moreover, we show that the zero-crossing feature of the DE has several characteristics that make it ideal for capacity estimation. Namely, the feature

1. is detectable at various practical C-rates up to 1C [14,16].
2. occurs within a frequently used operational SOC range (close to 50% SOC).
3. is unaffected by the initial SOC, so it can be used during charging.

The paper is organized as follows: Section 2 describes the experimental methodology and presents the range of aging conditions from charge/discharge C-rates, temperatures, and depth of discharges. Section 3 presents the experimental results, evolution, and correlation of the voltage and expansion signals with the capacity fade. The various differential signals are introduced. Using the experimental data, a number of features in expansion and voltage are identified. Linear regression models based on different combinations of experimentally observed features are developed. The accuracy and robustness of the different data-driven regression models are compared. The model based on the zero-crossing of the differential expansion feature is shown to be superior for the capacity fade estimation. Section 4 summarizes the contributions.

2. Experimental procedures

2.1. Cycling aging

A number of identical pouch cells were manufactured in one batch using the fabrication facility at the University of Michigan Battery Lab (UMBL) to study the degradation under various conditions. The production of the cells in one batch minimizes the cell-to-cell variation in performance caused by the manufacturing process [18]. The cells were comprised of graphite (Hitachi MAG-E3) anode and NMC 111 (TODA North America) cathode with the detailed specifications shown in Table 1. The cells were primarily designed as energy cells, which led to a relatively fast degradation at high charging rates [19], and enabled a faster study of different aging conditions. The cells were assembled inside the fixture and placed in a climate chamber shown in Fig. 1(a). The fixture, shown in Fig. 1(b), was designed such that the top and bottom plates are fixed in place while the middle plate is free moving. Compression springs were used to apply a prescribed pressure on the cell. Spring modulus was selected to be much lower than the battery, which ensures almost constant pressure on the cell as it cycles and expands. Initial target pressures of 34.5 kPa (5 psi) were achieved by adjusting the spring compression to a fixed displacement using the threaded rods. Furthermore, polymer poron sheets (Rogers, USA) were used on both sides of the pouch cell to achieve a more uniform pressure on the cell and avoid high-pressure spots. The expansion is measured using a displacement sensor (Keyence, Japan) mounted on the top plate similar to [16]. The precision and repeatability of the expansion measurement was checked by back-to-back C/10 charge and discharge cycles and found to be close to the sensor accuracy (Fig. S1). The measurement of expansion using load cells [5] and strain gauges [20,21] have also been shown previously and can be applied on a wider scale. The dynamic testing was carried using a battery cycler (Biologic, France). A climate chamber (Cincinnati Ind., USA) was used in order to control the temperature during cycling. The temperature was measured using a K-type thermocouple (Omega, USA) place on the battery's surface.

Table 1
Pouch cell specifications.

Pouch cell	
Nominal capacity	5.0 Ah
Operating voltage	3.0–4.2 V
Thickness	4.0 mm
Length	132 mm
Width	90 mm
Positive electrode	
Material	NMC111:CB:PVDF (94:3:3)
Number of double sided electrode sheets	14
Electrode active material loading	18.5 (single side) mg/cm^2
Electrode thickness	67 μm
Negative electrode	
Material	Graphite:PVDF (95:5)
Number of double sided electrode sheets	15
Electrode active material loading	8.55 (single side) mg/cm^2
Electrode thickness	62 μm
Separator	
Material	Polyethylene (PE)
Electrolyte	
Material	1 M $LiPF_6$
Organic solvent in electrolyte	3:7 EC:EMC v/v + 2wt% VC

The aging experiments were designed to cover an array of stress factors such as C-rates during charge and discharge, depth of discharges (DOD), and temperatures. Based on these stress factors, a number of testing conditions were selected. The summary of all the testing conditions is shown in Table 2. Each of the test conditions is done at three different temperatures of hot (45 °C), cold (−5 °C), and room (25 °C), which are indicated by condition group A to G. The condition group G utilizes a realistic daily drive cycle with fast charging for an electric vehicle. The details of the drive cycle are presented in Fig. S4. In the following, the C-rate noted for all the test procedures is defined with respect to the *nominal* cell capacity (i.e., 5 Ah).

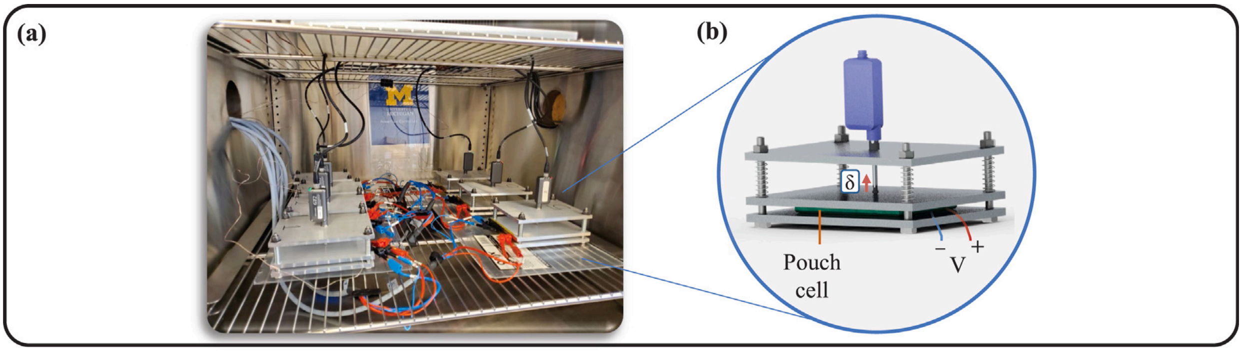

Fig. 1. (a) The testing configuration inside the climate chamber and (b) the schematic of the fixture.

Table 2
The aging test conditions matrix.

Cycling aging conditions				
Condition group	Cell number–Temperature (R/C/H)[a]	DOD	Charge[b]	Discharge
A – (baseline)	01 (R) | 02 (C) | 03 (H)	0%–100%	C/5	C/5
B	04 (R) | 05 (C) | 06 (H)	0%–100%	1.5C	1.5C
C – (fast charge)	07 (R) | 08 (C) | 09 (H)	0%–100%	2C	2C
D	10 (R) | 11 (C) | 12 (H)	0%–100%	C/5	1.5C
E	13 (R) | 14 (C) | 15 (H)	0%–50%	C/5	C/5
F	16 (R) | 17 (C) | 18 (H)	0%–50%	C/5	1.5C
G – (drive cycle)	19 (R) | 20 (C) | 21 (H)	0%–50%	1.5C	Drive cycle[c]

[a]The R, C, and H corresponds to room (25 °C), cold (−5 °C), and hot (45 °C) temperature.
[b]Constant current until 4.2 V and then constant voltage until ($I < C/50$).
[c]For the details on the drive cycle refer to the Fig. S4.

Cycling procedure. Before starting the cycling tests, the chamber temperature was set to the target temperature of the cycling test, and the cells were held at rest for 3 h to ensure thermal equilibrium. The cycling consists of a constant current (CC) charge until reaching 4.2 V, followed by a constant voltage (CV) phase at 4.2 V until ($I < C/50$). Then a CC discharge until reaching 3.0 V for the full range conditions. For partial DOD, the discharge time is with respect to the nominal capacity at all times (i.e., to obtain 50% DOD, 2.5 Ah are discharged from a completely charged state). During all the tests, in addition to the traditional signals of voltage, current, and temperature, the thickness changes (expansion) of the cell are also recorded. All the cells were cycled to at least 70% capacity retention, and reference performance tests (RPTs) were performed periodically.

RPTs. Fig. 2(a) shows the testing procedure consists of cycling and RPTs. Initial RPTs were done for all the cells before the start of the aging experiment. The subsequent RPTs were performed after a certain number of cycles corresponding to an expected 5% capacity loss for cycling aging tests. Before starting the tests, the cells were brought back to room temperature (25 °C) and held at rest for 3 h to ensure thermal equilibrium. The RPTs are as following:

1. A C/20 charge–discharge cycle consists of an initial C/5 discharge until reaching 3.0 V, followed by a CV phase at 3.0 V until ($|I| < C/50$) and 1 h rest to ensure the cell is fully discharged. Then a C/20 charge until reaching 4.2 V, followed by a CV phase at 4.2 V until ($I < C/50$) and 1 h rest. Then a C/20 discharge until reaching 3.0 V.
2. Hybrid pulse power characterization (HPPC) measurements at 10% SOC intervals. First, the cells are charged using C/2 CC until 4.2 V, followed by a CV at 4.2 V until ($I < C/50$) and 1/2 h rest. Then a C/2 CC discharge for an equivalent of 10% SOC discharge, where the discharge time was adjusted based on the prior capacity measurement (C/20) test—followed by a 1/2 h rest. Then the HPPC profile consisted of a 1C CC discharge for 10 s, a 10 min rest, a 1C CC discharge for 10 s—followed by a 10 min rest. The above steps were repeated until the end of discharge 3.0 V was reached.
3. The C-rate dependency test consists of charging the cell at different rates for characterizing the rate capabilities of the cell. Before each charge, the cell was fully discharged to 3.0 V by a C/3 discharge current until reaching 3.0 V, followed by a CV phase at 3.0 V until ($|I| < C/50$). Then the cell was charged using CC (C/10, C/5, C/2, and 1C) until 4.2 V. The voltage and expansion response are measured at various C-rates, as shown in Fig. 2(b). Then, the various differential signals are processed using filtering and a number of features are extracted as shown in Fig. 2(c).

Data filtering. The differential signals are processed using the Savitsky–Golay (SG) filtering technique [22]. In this filtering method, a polynomial is fitted to a moving frame of the data. Selecting a suitable polynomial order and data frame length depends on the noise levels and the number of available data points. Generally, lower-order polynomials and larger data frames lead to more filtering. In this work, the polynomial order of three is selected. The data acquisition frequency is fixed at 0.1 Hz. This means that charging at higher C-rates results in a fewer number of data points. It was discovered that a fixed SOC window for data frame size leads to more consistent filtering compared to a fixed number of data points. Therefore, for different C-rates, the frame length is always set to the number of data points equivalent to a 5% SOC window.

Initial SOC sensitivity test. A C/3 discharge to 5% SOC, followed by a 1 h rest. Then a charge with C/10 CC until 4.2 V, followed by a CV phase at 4.2 V until ($I < C/50$) and 1 h rest. The previous steps are repeated for a discharge to 20% and 40% SOC. The test is done again for the C/5, C/2, and 1C for the charge current. This test is done at the end of the cycling test.

2.2. Data and code availability

The datasets presented in this study are available at https://doi.org/10.7302/7tw1-kc35.

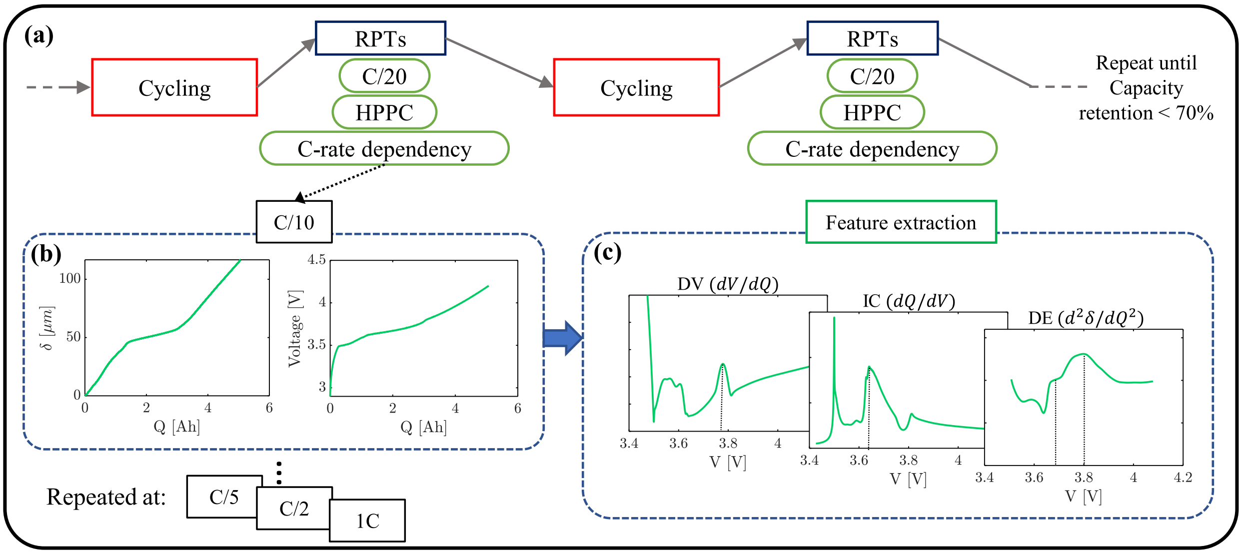

Fig. 2. (a) The testing procedure. The reference performance tests (RPTs) are done at approximately every 5% loss in capacity. The RPTs consist of a C/20 charge and discharge capacity measurement, the hybrid pulse power characterization (HPPC) test for measuring the resistance at various SOC states, and the c-rated dependency test of charging at various C-rates (C/10, C/5, C/2, 1C) from the discharged state. (b) A typical voltage and expansion measurement at C/10. (c) The incremental capacity (IC), differential expansion (DE), and voltage (DV) signals are extracted and filtered using the charging data. This processes is repeated for other C-rates of C/5, C/2, and 1C.

3. Results and discussion

3.1. Capacity fade

The capacity evolution of all the aging conditions is shown in Fig. 3. The aging conditions are also denoted in Fig. 3. The conditions consist of symmetrical and unsymmetrical cycling with C-rates from C/5 to 2C, room @25 °C, cold @ − 5 °C, hot @45 °C temperatures, and a full and 50% depth of discharge. The capacity fade measured using the C/20 RPT and the capacity fade measured during cycling are shown in Fig. 3(a) and (b), respectively. In this paper, the C/20 capacity measurement at 25 °C is used to quantify the maximum capacity of the cell and this capacity is referred to as the *thermodynamic* capacity of the cell. The thermodynamic capacity fade is primarily caused by LLI and LAM at each electrode [15]. On the other hand, the capacity measured during each cell's specific cycling conditions is affected by the C-rate via the resistive drop, diffusion limitations, and other effects such as cell temperature beyond the loss of active material (LAM) and loss of Lithium Inventory (LLI). We refer to this capacity as the *apparent* capacity of the cell because it is the observed (apparent) capacity which is the combined result of multiple phenomena. The low charging rate of C/20 minimizes the impact of resistance on the measured capacity. As a result, the C/20 capacity fade shown in Fig. 3(a) is denoted as the thermodynamic capacity fade, which is caused by the aging modes

Fig. 3(b) shows the apparent discharge capacity, which is measured at the C-rate and temperature that the cells were cycling. Therefore, depending on the C-rate, the resistance growth can also reduce the measured apparent capacity when the minimum voltage is reached sooner due to a larger ohmic voltage drop. The apparent capacity can be a more relevant measure of capacity in field applications, nevertheless, it can be easily inferred after estimating the thermodynamic capacity by measuring the resistance. The measurement of resistance is relatively easy and fast since, for example, it can be done with simple pulse charge techniques. In terms of capacity estimation, in this paper, the objective is the estimation of the thermodynamic capacity. Measurement of the thermodynamic capacity requires prolonged experiments that often can take days to finish. Moreover, the periodic thermodynamic capacity RPT disrupts the cycling aging and can have unintended consequences on the aging process, such as capacity recovery [23,24], which complicates the translation of lab data to the real-world aging scenarios. Therefore, methods that can estimate the thermodynamic capacity during cycling and accelerated conditions such as high C-rates are more difficult to obtain and the focus of our effort.

3.2. Expansion differential

The differential analysis is utilized in order to identify the prominent features in the expansion. The second differential of expansion (DE) with respect to charge displays distinct features such as local maximums and minimums. These features are the product of the various stages of phase transitions in the graphite anode [17]. The differential of voltage (DV) with respect to charge also exhibits similar features, and the connections of the DV and DE features to the graphite phase transitions have been reported previously [14,16]. The distinct features in the DV signal such as voltage level at the peaks and also features in the incremental capacity (IC), which is the inverse of DV, have been utilized in capacity estimation methods [6,9]. These features are often quantified using a fixed constant current during charge or discharge. This paper systematically compares the expansion and voltage features measured at various constant charge currents. Also, the impact of partial charging is quantified by varying the initial SOC during charging tests. In the following, the various signals based on differential analysis of the voltage and expansion measurements are introduced, and the features of interest are described.

Fig. 4(b) shows a measurement of the voltage and expansion during charging at C/10. In this case, the measurements are from cell 01 at the fresh state. The differential expansion (DE) is defined as the second derivative of the expansion, δ, with respect to the amount of input-charge, Q. The DE signal is plotted in Fig. 4(a). The differential voltage (DV) is defined as the derivative of the voltage, V, with respect to the amount of input-charge, Q. The DV signal is also plotted in Fig. 4(a). Notably, in the DE and DV signals a peak is observable at the same location near 60% SOC, 3.8 V, verifying that these features are fundamentally pointing towards the same graphite phase transitions. Lastly, the incremental capacity (IC) is defined as the derivative of the amount of input-charge, Q, with respect to voltage, V (i.e., the inverse of the DV). The IC signal is plotted in Fig. 4(c). The peaks in the IC signal correspond to the local minimums in the DV signal. Here, the signals are plotted on the x-axis, and the voltage is plotted on the y-axis. This is to aid in illustrating the location of the features in the voltage curve and their corresponding SOC values.

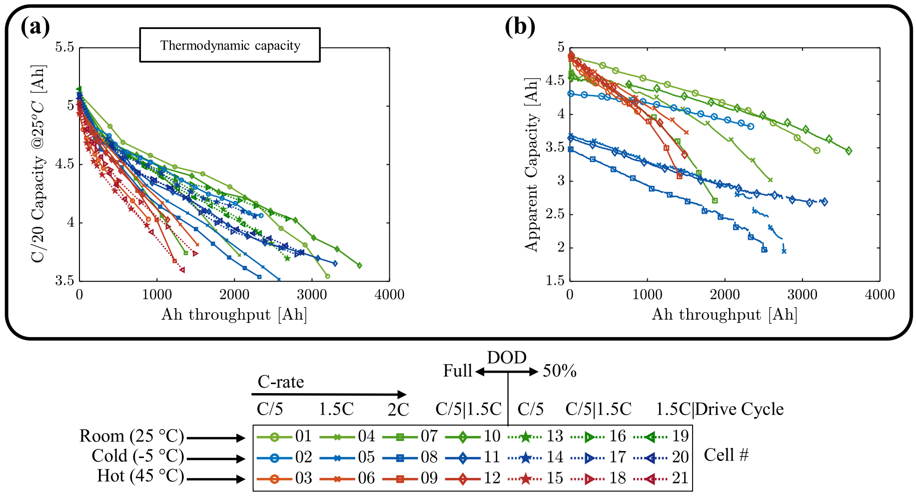

Fig. 3. (a) The thermodynamic capacity measured during the periodic C/20 tests at 25 °C, which is computed by averaging the charge and discharge capacities. The C/20 capacity is plotted for all the aging conditions versus Ah throughput. (b) The apparent discharge capacity measured during cycling. The apparent capacity is only available for the cell with a full DOD, namely cells 1–12.

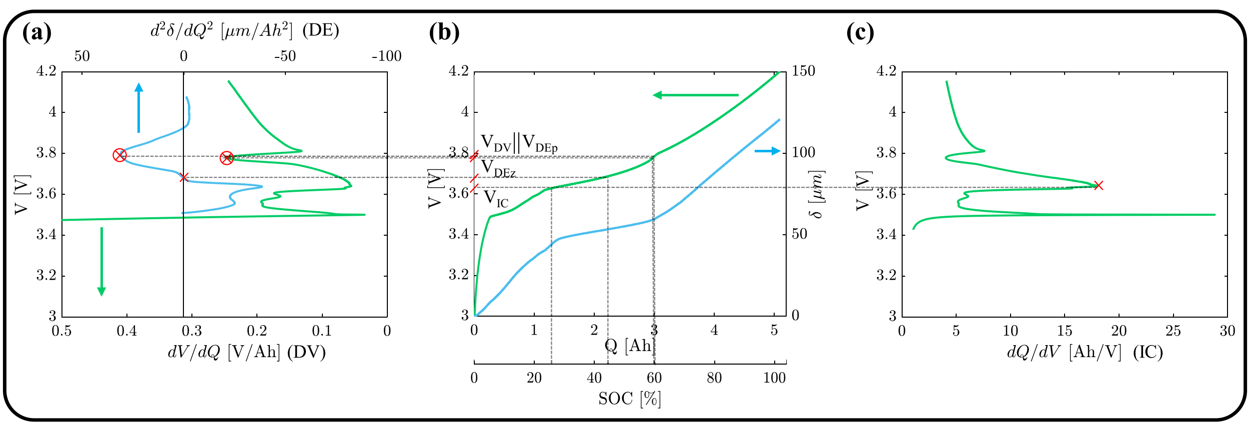

Fig. 4. (a) The differential voltage and expansion. (b) The voltage and expansion during charging at C/10. (c) The incremental capacity. The selected feature in differential voltage (DV) is the voltage at the peak observed about the 60% SOC. The selected feature in differential expansion (DE) is the voltage at the zero cross over point observed about the 45% SOC. The selected features in incremental capacity (IC) are the voltage and the height of the peak observed about the 25% SOC.

As can be seen from Fig. 4(a) and (c), several distinct features can be used for each of the signals. For example, the measured voltage at any of the peaks or their height. Nevertheless, the most important criteria for selecting a feature is its correlation factor with capacity fade. In other words, the feature should maintain a strong correlation with capacity retention that is invariant to the cycling conditions. Furthermore, the feature needs to be insensitive to the initial SOC at the start of charging, and the correlation should remain strong at various C-rates. It is also desirable that the feature appears at SOC ranges that most electric or hybrid vehicles usually operate in, meaning the feature should not occur at a high depth of discharge (SOC $<$ 20%). These conditions are essential for the relevance of the capacity estimation method for real-world applications.

Several prominent features are selected, which are marked in Fig. 4(a) and (c). For the IC signal, the measured voltage, V_{IC}, at the peak occurring about 25% SOC and its height, H_{IC} are selected. For the DE signal, the measured voltage, V_{DEp}, at the peak, occurring about 60% SOC and the zero crossover point ($d^2\delta/dQ^2 = 0$), V_{DEz}, occurring about 45% SOC are selected. A second zero-crossing point is also available at a higher SOC and voltage in Fig. 4(a), however, this point is not consistently detectable at various C-rate and aged states. On the other hand, the selected zero-crossing point (close to 45% SOC) is well observable even at the most aged states, and corresponds to the center of the middle plateau in the graphite potential. For the DV signal, the measured voltage, V_{DV}, at the peak, occurring about 60% SOC is selected. The summary of all the signals and features are shown in Table 3. In the following sections, the correlation of these features with capacity and their sensitivity to the charge conditions are presented.

3.3. Evolution of the differential signals at different C-rates

As an example, the evolution of the DE, DV, and IC signals of cell 04 (1.5C/1.5C @25 °C) during aging is shown in Fig. 5(a), (b), and (c), respectively. For each signal, the evolution is shown for the C/10, C/5, C/2, and 1C. The lines in Fig. 5 are colored from green to red for fresh to aged. Note that in Fig. 5(b) the height of the DV peak diminishes considerably at 1C, which makes detection of this peak infeasible. The diminishing height of the DV peak with increased C-rate is a well understood phenomenon [14] and has been attributed and reproduced with electrochemical models that capture the non-uniform charging of the graphite across electrodes [16]. It is also observable that all signals are shifting to higher voltages with aging. This change is about 60 mV for the C/10 rate and about 100 mV for the 1C rate at the maximum. The resistance increase is partially responsible for this change.

The direct current resistance (DCR) is calculated using the HPPC data. Dividing the voltage drop after 1 s after each discharge and charge pulse by the current magnitude of 1C (5 A) gives the resistance values in discharge and charge direction. The discharge and charge resistances

Table 3
The summary of the different features and signals.

Signal	Feature	Definition
DE ($d^2\delta/dQ^2$)	V_{DEz}	The measured voltage at the zero-crossing point about the 45% SOC
	V_{DEp}	The measured voltage at the local maximum about the 60% SOC
DV (dV/dQ)	V_{DV}	The measured voltage at the local maximum about the 60% SOC
IC (dQ/dV)	V_{IC}	The measured voltage at the local maximum about the 25% SOC
	H_{IC}	The magnitude of the IC signal at the local maximum about the 25% SOC, i.e. V_{IC} peak height

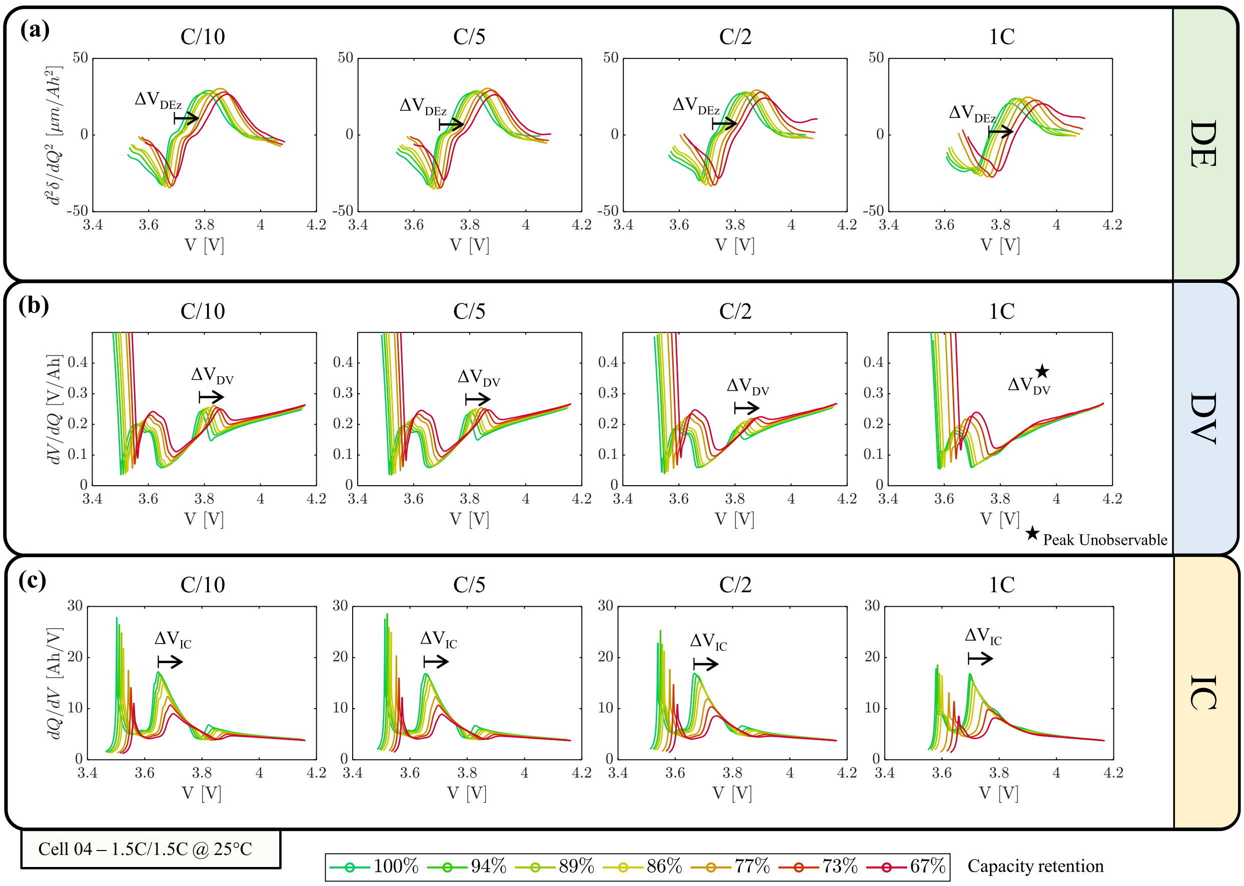

Fig. 5. (a) The evolution of the differential expansion (DE), (b) the differential voltage (DV), and (c) the incremental capacity (IC) signals for the cell 04 (1.5C/1.5C @25 °C) at various C-rates during aging. Note that the peak in DV is unobservable at 1C. The lines are color coded from green (fresh) to red (most aged). (For interpretation of the references to color in this figure legend, the reader is referred to the web version of this article.)

are calculated at 10% SOC intervals and averaged to estimate the DCR. For reporting the resistance increase during aging, the average value of the DCRs over the whole SOC range is used. Fig. S2(a) shows the average DCR increases for all the aging conditions. The resistance increase is faster for the cells cycled at the hot temperature. The resistance increase varies significantly with the aging conditions and the operating temperature. On average, the resistance was increased by 100% at the end of cycling (70% capacity retention), going from 8 mΩ to 16 mΩ.

A resistance increase of about 8 mΩ translates to a 4 mV and 40 mV shift for all signals (DE, DV, and IC) due to resistance increase at C/10 and 1C, respectively, in Fig. 5. Therefore, at low C-rates, the impact of the resistance increase is much lower on the voltage shift, and in fact, the majority of the voltage shift is due to the underlying degradation of individual electrodes. It is also worth noting that in the experimental IC signals of Fig. 5(c), the height of the peak in the IC signal decreases with aging. This is expected as the area under the IC curve is equal to charge capacity. Therefore, overall the IC curve magnitude should decrease with aging.

3.4. Sensitivity of the differential signals during charging to different initial SOCs

The goal here is to assess the sensitivity of the signals (and their features) to the initial SOC of the charge. As in practice, the charging process can start from different initial SOCs. The test was performed after the termination of the cycling experiment with the cell at approximately 70% capacity retention (see Section 2 for detailed steps). The experiment was done with respect to three different initial SOC of 5%, 20%, and 40%, and was repeated with various C-rates. The results of this experiment for cell 04 are presented in Fig. 6. The DE, DV, and IC signals at various C-rates are shown in Fig. 6(a), (b), and (c), respectively. For the DE signal, the zero crossover point is detectable with 5% and 20% initial SOC. The voltage values of this feature, V_{DEz}, are presented in Table S1 with the maximum error of 5 mV observed at 1C. However, large deviations are observable for the location, V_{DEp}, and height of the DE peak.

In Fig. 6(b), for the DV signal the peak is detectable with 5%, 20%, and 40% initial SOC. Similar to the results of Fig. 5(b), which has a charge starting from a full depth of the discharge, the peak is still not

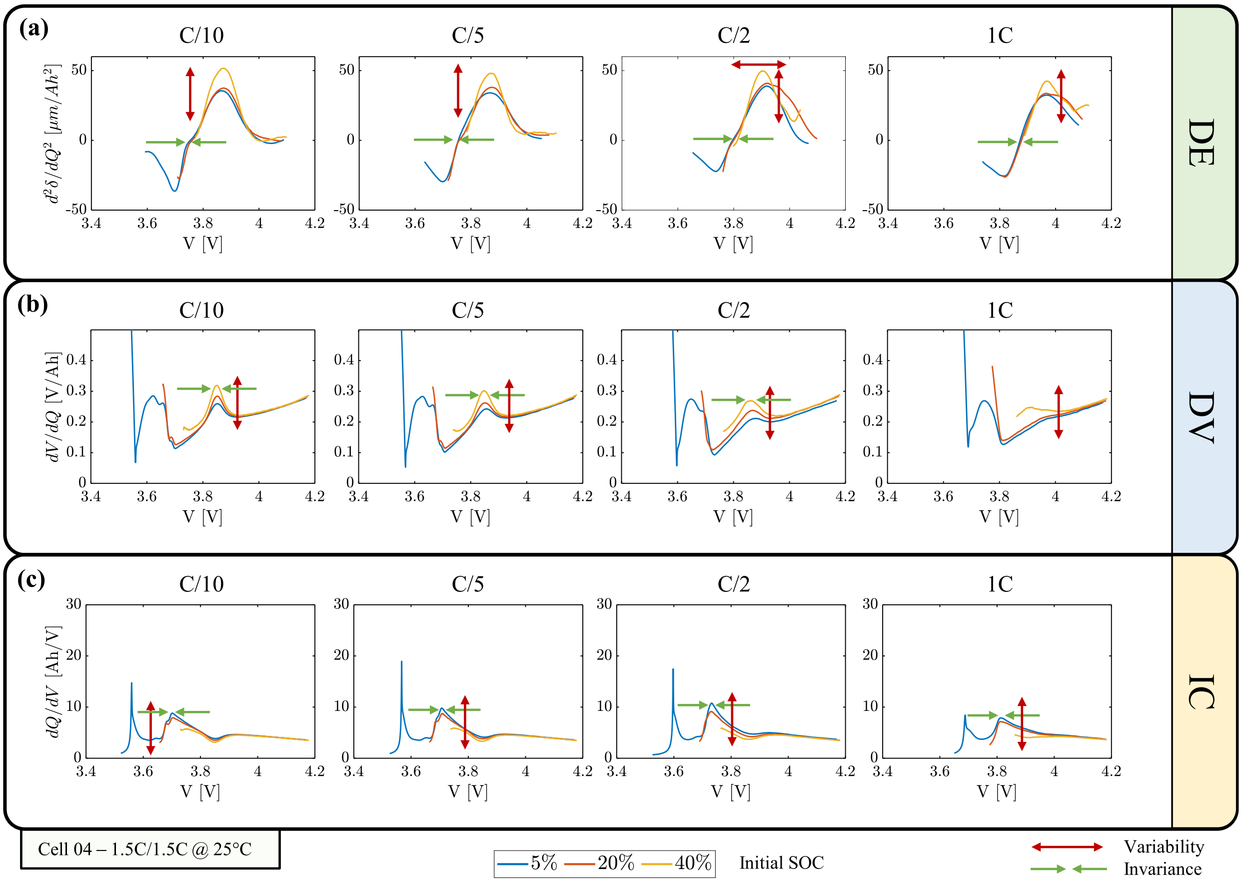

Fig. 6. The data shown is taken at the end of life near 67% capacity retention. (a) The charge response of the DE, (b) DV, and (c) IC signals with respect to the initial SOC at various C-rates. The signals are plotted for the 5%, 20%, and 40% initial SOC. Note that the height of the peaks in DE, DV, and IC curve varies greatly depending on the initial SOC. The location of the peak in the DV and IC signals is consistence regardless of the initial SOC. Moreover, the zero crossover point of the DE signal also remains unchanged by the initial SOC.

observable at 1C. The voltage values of the peak, V_{DV}, at lower C-rates are available in Table S2 with a maximum error of 5 mV observed at C/2. Nevertheless, similar to the DE peak, a large variation of the peak height is observed depending on the initial SOC. The peak in IC signal in Fig. 6(c) is detectable with 5% and 20% initial SOC. The voltage values, V_{IC}, of the peak, are presented in Table S3 with the maximum error of 2 mV observed at 1C. Here as well, the height of the peak, H_{IC}, changes with respect to the initial SOC.

3.5. Correlations between differential signal features and capacity

As noted in Fig. 4 the primary features selected in this study are the voltage at the peak of the DV and IC signals and zero crossover voltage of the DE signal. Other potential features are the height of the peaks in the DV and IC signals. However, as discussed earlier, the heights of these peaks are sensitive to the initial SOC, and therefore not suitable for robust capacity estimation. The features that appear only below 20% SOC were also not considered since to observe these features, a high depth of discharge is required. Additionally, the peak in the DE signal was also not robust with respect to the initial SOC. It should be mentioned that the evolution of the IC peak height and the voltage of the DE peak also shows a good degree of correlation with the capacity (see Fig. S3). However, due to the sensitivity of these features to the initial SOC, these features are not considered for the development of capacity estimation methods.

Fig. 7 shows the evolution of the selected features during aging for all the aging conditions. All three features have a good correlation with capacity. Similar to Fig. 3(a), the capacity in Fig. 7 is measured during the C/20 diagnostic test. Based on these results, each of the features are a good candidate for a capacity estimation method. Comparing the DV feature in Fig. 7(b) with the other two features, it is evident that there is larger distribution in the evolution of this feature among the aging conditions. In order to compare the accuracy of estimating capacity using the identified expansion and voltage features, linear regression models are fitted to the data.

From the results in Fig. 7, it is clear that the selected features have a strong correlation with the capacity that is highly independent of the vast array of aging conditions tested in this study. Thus, these features are great candidates for developing capacity estimation methods based on simple linear regression models. Furthermore, it is possible to combine these features to develop more robust capacity estimation methods. Therefore, various combinations of the features are also considered. In order to assess the goodness of the linear regression models, the root mean square error (RMSE) of the fits are compared. The RMSE is normalized by the nominal capacity of 5 Ah and is akin to an absolute error in estimating SOH. The linear regression models are fitted using all the data at each C-rate independently. The detailed results of the fitting for the C/5 and 1C are shown in Table 4. The DCR data is also used as a feature to develop a linear regression model and the results are reported in Table 4.

In terms of single features, the expansion feature, V_{DEz}, at 1C has the lowest absolute error of 1.9% for capacity estimation. Additionally, this feature remains observable up to 1C and occurs at about 50% SOC. At C/5, the combination of the V_{DEz} with V_{IC}, improves the accuracy of the capacity estimation method considerably. As can be seen from the results in Table 4 the combination of all the features has the best correlation with the capacity. However, as noted previously, the DV feature is not observable at 1C. Therefore, capacity estimation models

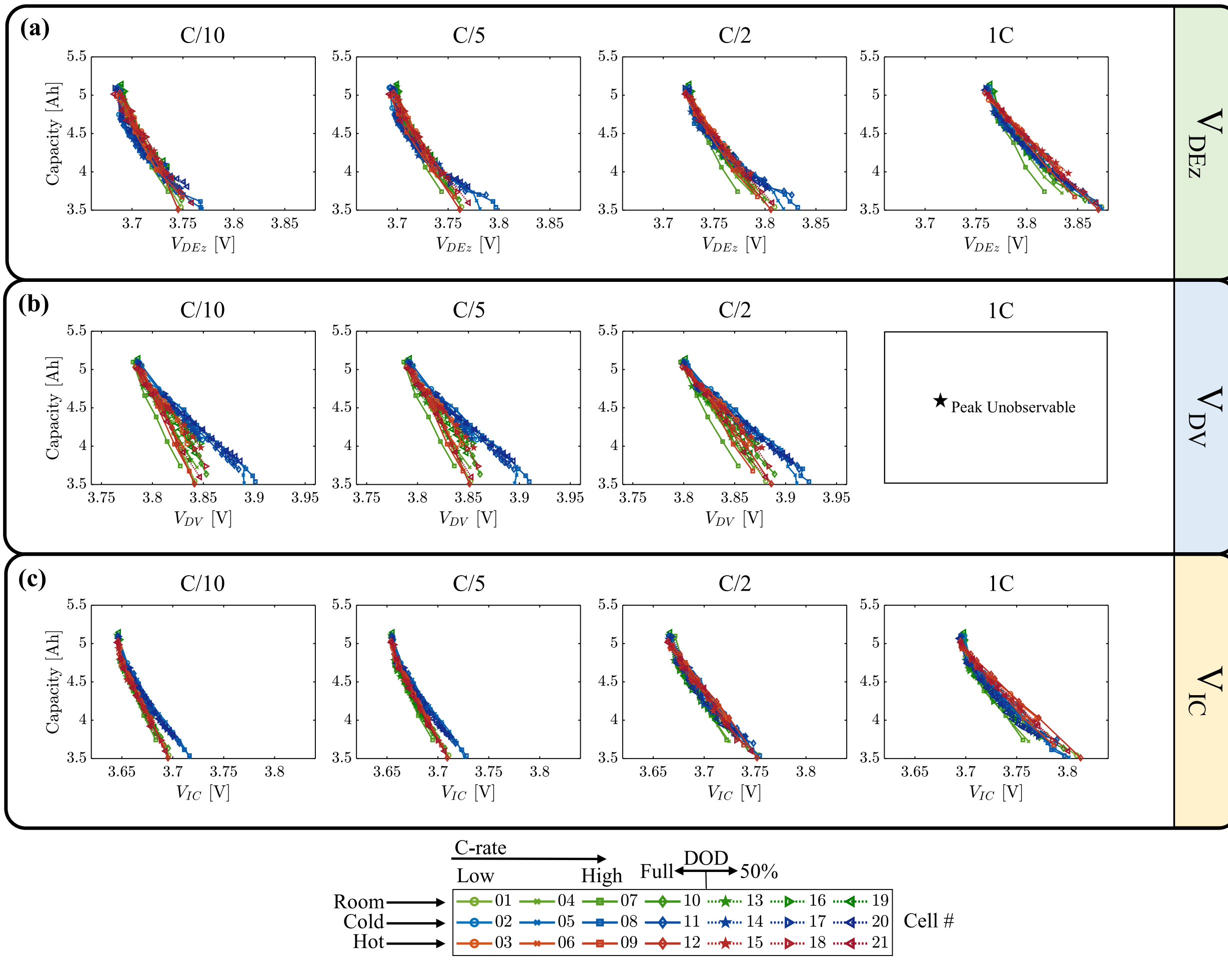

Fig. 7. (a) The evolution of the DE feature, V_{DEz}, (b) the DV feature, V_{DV}, and (c) the IC feature, V_{IC}, for all the aging conditions. The evolution of the features are plotted for different C-rates. At 1C the DV feature was not detectable, therefore, this C-rate is not included in the plot. The data is color coded such that the red, blue, and green colors correspond to the aging condition at hot, cold, and room temperatures, respectively. (For interpretation of the references to color in this figure legend, the reader is referred to the web version of this article.)

Table 4
RMSE values of the linear regression fit using different feature sets for all the conditions.

Features	RMSE/Q_{nom} [%]		Required SOC range
	C/5	1C	
V_{DV}	3.57	–	55%–65%
V_{DEz}	2.68	1.94	40%–50%
V_{IC}	2.36	2.21	20%–30%
V_{DV}, V_{IC}	2.28	–	20%–65%
V_{IC} , V_{DEz}	2.26	1.95	20%–50%
V_{DV}, V_{DEz}	2.54	–	40%–65%
V_{DV}, V_{IC}, V_{DEz}	2.22	–	20%–65%
DCR	4.17		–

with the DV features are only possible if the charging C-rates are below C/2. The required SOC range is also essential for the applicability of the estimation method for fast characterization. Methods that require shorter SOC ranges, rely on features from the middle of the entire SOC range, and are applicable at 1C are more desirable. In this sense, the expansion feature, V_{DEz}, fulfills all the aforementioned requirements.

As evident from the results of Table 4, capacity estimation using DCR has a large error since the evolution of average DCR is strongly dependent on the cycling conditions. The correlation of average DCR and capacity is shown in Fig. S2(b). On the other hand, measurement of the resistance can effectively be done at any SOC by applying a prescribed short-duration charge or discharge pulse. Nevertheless, particular attention to the effects of aging conditions is needed if one wants to utilize DCR reliably for capacity estimation.

Finally, it should be noted that in order to develop capacity estimation methods for cells with different chemistry or construction, it is necessary to collect the aging data. However, as demonstrated in this study, the correlation of the voltage and expansion features in Table 4 with capacity is largely independent of the aging conditions. Therefore, the data collection can be done using an accelerated aging condition like the (2C/2C) at hot temperature to significantly reduce testing time.

3.6. Origins of the differential signal shift from the mechanistic model perspective

As mentioned earlier, the capacity fade is due to the LLI and LAM. Often the capacity fade is significantly more at the negative electrode compared to the positive electrode. This is because the LLI is mainly due to side reactions of SEI growth and lithium plating at the negative electrode (graphite). Furthermore, the LAM can occur with particle cracking, separation, and isolation [15]. Particle cracking exposes fresh surface area to the electrolyte, which creates newly formed SEI layers. Therefore, the main reason for the increase in SEI growth is due to the increase in particle cracking [25]. Graphite is considered a brittle material, which means that the increase and decrease of the internal stresses during cycling can lead to the growth of cracks, fatigue failure, and ultimately material separation. High charge–discharge rates lead to large stress gradients in the particles, which propagates the micro-crack

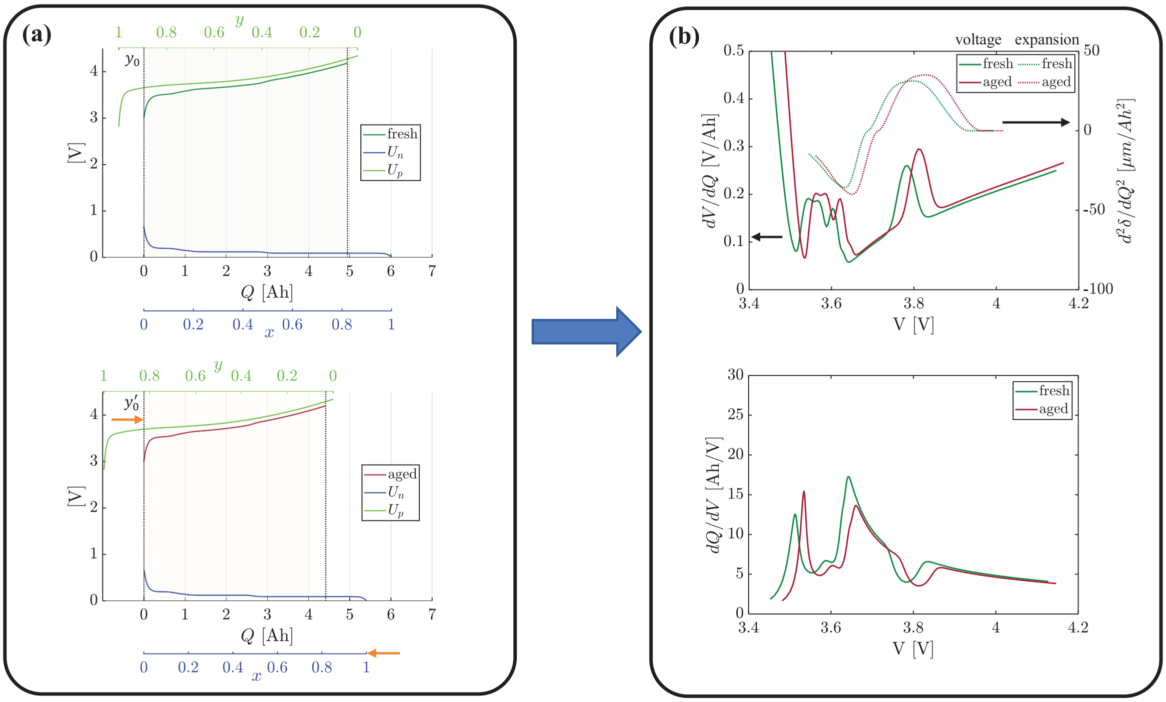

Fig. 8. (a) Mechanistic model of the changes to the OCV during aging. Notice the shift of the operating window of the positive electrode to higher potentials. (b) The DV, DE, and IC signals of the fresh and aged states. The aged signals are moved to a higher voltages.

formations. The temperature rise is also more significant at high C-rate than low C-rate conditions, which induces more SEI growth.

The LLI and LAM over the lifetime of the battery alter the open circuit voltage (OCV). The measured OCV is equal to the potential difference of the positive (U_p) and negative (U_n) electrodes. The specific shape of the OCV curve is a function of the operating stoichiometric window and the relative capacity of the electrodes, which evolves during aging depending on the amount of LLI and LAM. Fig. 8(a) shows a simulation of the OCV change during aging due to LLI and LAM. For this simulation study, the modeling methodology of Ref. [17] is utilized. Furthermore, the potential functions of the negative and positive electrodes are taken from Ref. [16]. In this simulation scenario, the LAM at the negative electrode is 11%, the LAM at the positive electrode is 5%, and the LLI is 9%, resulting in 10% capacity fade. The LAM at the negative electrode and LLI caused a shift of the stoichiometric window of the positive electrode (y_0) to higher potentials. As a result, as shown in Fig. 8(b), the DV, DE, and IC signals are moved to a higher voltage at the aged state. Therefore, in essence, the shift in the DV, IC, and DE signals to higher voltages is caused by the underlying degradation of individual electrodes during aging. Hence, the strong correlation of the features in the Table 4 with capacity fade is contributed to the interplay of the different degradation modes under the wide range of aging conditions.

4. Conclusion

In this paper, aging experiments were carried out, and the cell voltage and mechanical response were recorded under a variety of aging conditions such as C-rate and temperature. To develop a capacity estimation method based on voltage and expansion, the charge response of the cell was recorded periodically with different C-rates. It was demonstrated that with the expansion the diagnostics can be performed with a reduced SOC range, which speeds up the characterization considerably. The features in the DV, IC, and DE signals and their evolution with capacity fade were presented. Based on the results of sensitivity of the feature with respect to the initial SOC, a number of features were selected for developing capacity estimation methods. Different linear regression models were fitted to the data by considering all the combinations of the features. It was discovered that utilizing the IC and DE features results in the best method for capacity estimation in terms of accuracy. Furthermore, the expansion feature occurs in the middle of the SOC range, which makes it more useful for in-the-field applications as well. There are still several challenges that need to be addressed in future work. The sensitivity of the features to the operating temperature was not explored in this study and needed to be addressed. Also, the instrumentation of the batteries with expansion sensors remains an open issue in large packs. Nevertheless, the goal here was to demonstrate how the diagnostics can benefit by incorporating the expansion measurements technology. Additionally, the batteries can benefit from monitoring the expansion in other areas such as safety [26] and pressure control for future battery technologies that further encourages the inclusion and development of expansion sensors in future battery packs. For example, for the next generation anode materials with Si/C composites, the cycle life of these cells is highly dependent on the external pressure [25], and for solid-state batteries with lithium metal as the anode, it is necessary to account for the changes in cell expansion during charging and discharging due to Li plating and stripping, along with the changes during aging and preventing accelerated aging by adjusting the applied pressure [27].

CRediT authorship contribution statement

Peyman Mohtat: Conducted the experiments and analyzed the data, Wrote the manuscript, Editing the manuscript. **Suhak Lee:** Conducted the experiments and analyzed the data, Editing the manuscript. **Jason B. Siegel:** Conceived and supervised the project, Editing the manuscript. **Anna G. Stefanopoulou:** Conceived and supervised the project, Editing the manuscript.

Declaration of competing interest

The authors declare that they have no known competing financial interests or personal relationships that could have appeared to influence the work reported in this paper.

Acknowledgment

The experimental work in this study was thanks to the support of the Automotive Research Center (ARC) in accordance with Cooperative Agreement W56HZV-14-2-0001 U.S. Army CCDC GVSC. P.M., J.S. and A.S. also acknowledge funding from the National Science Foundation under Grant No. 1762247. This work was performed in part at the University of Michigan Battery Lab, Energy Institute, and the authors would like to thank Greg Less for his assistance on pouch cell fabrication. The authors would also like to thank Yi Ding, and Matt Castanier of GVSC. Distribution A. Approved for public release; distribution unlimited. (OPSEC 5301)

Appendix A. Supplementary figures and tables

Supplementary material related to this article can be found online at https://doi.org/10.1016/j.jpowsour.2021.230714.

References

[1] M. Woody, M. Arbabzadeh, G.M. Lewis, G.A. Keoleian, A. Stefanopoulou, Strategies to limit degradation and maximize Li-ion battery service lifetime-Critical review and guidance for stakeholders, J. Energy Storage 28 (2020) 101231, http://dx.doi.org/10.1016/j.est.2020.101231.

[2] G.L. Plett, Dual and joint EKF for simultaneous SOC and SOH estimation, in: Proceedings of the 21st Electric Vehicle Symposium (EVS21), Monaco, 2005, pp. 1–12.

[3] S.J. Moura, M. Krstic, N.A. Chaturvedi, Adaptive PDE observer for battery SOC/SOH estimation, in: Dynamic Systems and Control Conference, Vol. 45295, American Society of Mechanical Engineers, 2012, pp. 101–110, http://dx.doi.org/10.1115/DSCC2012-MOVIC2012-8800.

[4] S.-C. Huang, K.-H. Tseng, J.-W. Liang, C.-L. Chang, M.G. Pecht, An online SOC and SOH estimation model for lithium-ion batteries, Energies 10 (4) (2017) 512, http://dx.doi.org/10.3390/en10040512.

[5] S. Mohan, Y. Kim, A.G. Stefanopoulou, Estimating the power capability of Li-ion batteries using informationally partitioned estimators, IEEE Trans. Control Syst. Technol. 24 (5) (2016) 1643–1654, http://dx.doi.org/10.1109/TCST.2015.2504847.

[6] I. Bloom, A.N. Jansen, D.P. Abraham, J. Knuth, S.A. Jones, V.S. Battaglia, G.L. Henriksen, Differential voltage analyses of high-power, lithium-ion cells: 1. Technique and application, J. Power Sources 139 (1–2) (2005) 295–303, http://dx.doi.org/10.1016/j.jpowsour.2004.07.021.

[7] X. Feng, Y. Merla, C. Weng, M. Ouyang, X. He, B.Y. Liaw, S. Santhanagopalan, X. Li, P. Liu, L. Lu, et al., A reliable approach of differentiating discrete sampled-data for battery diagnosis, ETransportation 3 (2020) 100051, http://dx.doi.org/10.1016/j.etran.2020.100051.

[8] C. Weng, J. Sun, H. Peng, Model parametrization and adaptation based on the invariance of support vectors with applications to battery state-of-health monitoring, IEEE Trans. Veh. Technol. 64 (9) (2014) 3908–3917, http://dx.doi.org/10.1109/TVT.2014.2364554.

[9] X. Li, Z. Wang, L. Zhang, C. Zou, D.D. Dorrell, State-of-health estimation for Li-ion batteries by combing the incremental capacity analysis method with grey relational analysis, J. Power Sources 410 (2019) 106–114, http://dx.doi.org/10.1016/j.jpowsour.2018.10.069.

[10] S. Lee, P. Mohtat, J.B. Siegel, A.G. Stefanopoulou, J.-W. Lee, T.-K. Lee, Estimation error bound of battery electrode parameters with limited data window, IEEE Trans. Ind. Inf. 16 (5) (2019) 3376–3386, http://dx.doi.org/10.1109/TII.2019.2952066.

[11] N.A. Samad, Y. Kim, J.B. Siegel, A.G. Stefanopoulou, Battery capacity fading estimation using a force-based incremental capacity analysis, J. Electrochem. Soc. 163 (8) (2016) A1584, http://dx.doi.org/10.1149/2.0511608jes.

[12] S. Mohan, Y. Kim, J.B. Siegel, N.A. Samad, A.G. Stefanopoulou, A phenomenological model of bulk force in a li-ion battery pack and its application to state of charge estimation, J. Electrochem. Soc. 161 (14) (2014) A2222, http://dx.doi.org/10.1149/2.0841414jes.

[13] M.A. Figueroa-Santos, J.B. Siegel, A.G. Stefanopoulou, Leveraging cell expansion sensing in state of charge estimation: Practical considerations, Energies 13 (10) (2020) 2653, http://dx.doi.org/10.3390/en13102653.

[14] Z.J. Schiffer, J. Cannarella, C.B. Arnold, Strain derivatives for practical charge rate characterization of lithium ion electrodes, J. Electrochem. Soc. 163 (3) (2015) A427–A433, http://dx.doi.org/10.1149/2.0091603jes.

[15] C.R. Birkl, M.R. Roberts, E. McTurk, P.G. Bruce, D.A. Howey, Degradation diagnostics for lithium ion cells, J. Power Sources 341 (2017) 373–386, http://dx.doi.org/10.1016/j.jpowsour.2016.12.011.

[16] P. Mohtat, S. Lee, V. Sulzer, J.B. Siegel, A.G. Stefanopoulou, Differential expansion and voltage model for Li-ion batteries at practical charging rates, J. Electrochem. Soc. 167 (11) (2020) 110561, http://dx.doi.org/10.1149/1945-7111/aba5d1.

[17] P. Mohtat, S. Lee, J.B. Siegel, A.G. Stefanopoulou, Towards better estimability of electrode-specific state of health: Decoding the cell expansion, J. Power Sources 427 (2019) 101–111, http://dx.doi.org/10.1016/j.jpowsour.2019.03.104.

[18] K. Rumpf, M. Naumann, A. Jossen, Experimental investigation of parametric cell-to-cell variation and correlation based on 1100 commercial lithium-ion cells, J. Energy Storage 14 (2017) 224–243, http://dx.doi.org/10.1016/j.est.2017.09.010.

[19] R. Zhao, J. Liu, J. Gu, The effects of electrode thickness on the electrochemical and thermal characteristics of lithium ion battery, Appl. Energy (ISSN: 0306-2619) 139 (2015) 220–229, http://dx.doi.org/10.1016/j.apenergy.2014.11.051.

[20] A. Knobloch, C. Kapusta, J. Karp, Y. Plotnikov, J.B. Siegel, A.G. Stefanopoulou, Fabrication of multimeasurand sensor for monitoring of a li-ion battery, J. Electron. Pack. 140 (3) (2018) http://dx.doi.org/10.1115/1.4039861.

[21] L.K. Willenberg, P. Dechent, G. Fuchs, D.U. Sauer, E. Figgemeier, High-precision monitoring of volume change of commercial lithium-ion batteries by using strain gauges, Sustainability 12 (2) (2020) 557, http://dx.doi.org/10.3390/su12020557.

[22] A. Savitzky, M.J. Golay, Smoothing and differentiation of data by simplified least squares procedures, Anal. Chem. 36 (8) (1964) 1627–1639.

[23] A. Eddahech, O. Briat, J.-M. Vinassa, Lithium-ion battery performance improvement based on capacity recovery exploitation, Electrochim. Acta 114 (2013) 750–757, http://dx.doi.org/10.1016/j.electacta.2013.10.101.

[24] B. Epding, B. Rumberg, H. Jahnke, I. Stradtmann, A. Kwade, Investigation of significant capacity recovery effects due to long rest periods during high current cyclic aging tests in automotive lithium ion cells and their influence on lifetime, J. Energy Storage 22 (2019) 249–256, http://dx.doi.org/10.1016/j.est.2019.02.015.

[25] A. Louli, L. Ellis, J. Dahn, Operando pressure measurements reveal solid electrolyte interphase growth to rank Li-Ion cell performance, Joule 3 (3) (2019) 745–761, http://dx.doi.org/10.1016/j.joule.2018.12.009.

[26] T. Cai, S. Pannala, A.G. Stefanopoulou, J.B. Siegel, Battery internal short detection methodology using cell swelling measurements, in: 2020 American Control Conference (ACC), IEEE, 2020, pp. 1143–1148, http://dx.doi.org/10.23919/ACC45564.2020.9147956.

[27] K.B. Hatzell, X.C. Chen, C.L. Cobb, N.P. Dasgupta, M.B. Dixit, L.E. Marbella, M.T. McDowell, P.P. Mukherjee, A. Verma, V. Viswanathan, et al., Challenges in lithium metal anodes for solid-state batteries, ACS Energy Lett. 5 (3) (2020) 922–934, http://dx.doi.org/10.1021/acsenergylett.9b02668.